Structural and spectroscopic studies of NaCuCr2(PO4)3: a noncentrosymmetric phosphate belonging to the α-CrPO4-type compounds

Khalifa Souiwa, Eric Lebraud, Marion Gayot, François Weill, Fabrice Mauvy, Maxim Avdeev, Radhouane Chtourou, Mourad Hidouri, Olivier Toulemonde

Structural and spectroscopic studies of $NaCuCr_2(PO_4)_3$: a noncentrosymmetric phosphate belonging to the α-$CrPO_4$ type compounds

Khalifa Souiwa[a, b*], Eric Lebraud[c], Marion Gayot[d], Francois Weill[c], Fabrice Mauvy[c], Maxim Avdeev[e, f], Radhouane Chtourou[b], Mourad Hidouri[a] and Olivier Toulemonde[c*]

[a] *Laboratoire Physico-Chimie de Matériaux, Faculté des Sciences, Université de Monastir, 5019, Monastir, Tunisie.*

[b] *Centre de Recherches et des Technologies de l'Energie. Technopole de Borj-Cédria - B.P. 95,* 2050 *Hammam-Lif. Tunisie*

[c] *CNRS, Université de Bordeaux, ICMCB, 87 avenue du Dr. A. Schweitzer, Pessac, F-33608, France.*

[d] *CNRS, Univ. Bordeaux, PLACAMAT UMS 3626, Pessac, F-33600, France*

[e] *Australian Centre for Neutron Scattering, Australian Nuclear Science and Technology Organisation, Sydney, Australia*

[f] *School of Chemistry, The University of Sydney, Sydney, Australia*

**corresponding authors khalifa.souiwa@gmail.com and olivier.toulemonde@icmcb.cnrs.fr*

Abstract

An electron and joint neutron and X-ray diffraction study of the synthetic copper / chromium phosphate $NaCuCr_2(PO_4)_3$ (NaCuP) is reported. A noncentrosymmetric *Imm*2 space group belonging to the well known α-$CrPO_4$ type is observed contrary to what is reported in $NaMCr_2(PO_4)_3$ (M = Co and Ni) phosphates. The structural model is validated by bond-valence-sums (BVS) and charge-distribution (CHARDI) calculations and supported by complementary Infra Red and Raman spectroscopy investigations. Both Raman spectroscopy and theoretical study by deformation density approach further suggest the presence of Cu^{2+} ($3d^9$) and Cr^{2+} ($3d^4$) Jahn-Teller polaron effect as key factor to the centro *Imma* to non-centro-symmetric *Imm*2 phase change.

1. Introduction

Since the lithium phosphate compound $LiFePO_4$ was proposed as a promising candidate for new generation of materials for energy storage applications with its advantages of being environmentally benign and safe[1, 2], the research in the field of open-framework inorganic materials with higher stability have extended dramatically and attracted the attention of a lot of researchers, during the last decades. Lithium-ion batteries were among the most performing battery technologies in terms of energy storage even if the known difficulty is the scarcity of lithium resources regarding the demand. In this context, the sodium element represents a promising solution. Indeed lithium and sodium atomic and electrochemical properties i.e. redox potential, atomic weight, ion size and valence are quite similar. Therefore, Na^+-ion batteries start to be an alternative to lithium-ion batteries, due to the abundance and cost effectiveness of sodium element[3–5]. A sodium-ion battery that holds as much energy and works as well as some commercial lithium-ion battery chemistries has indeed been optimized recently[6].

In parallel to investigations for anode materials for sodium-ion batteries[6,7,8], a systematic study of alkali mixed transition metal phosphates compounds has been initiated for their magnetic properties. They are related to the α-$CrPO_4$ type structure[9] and belonging to the Na_2O-$M^{II}O$-Cr_2O_3-P_2O_5 systems where M a divalent transition metal cation. Among other experimental results, a spin flop transition at 32K in $NaCoCr_2(PO_4)_3$ compound due to the magnetic superexchange interaction competitions were reported[10] as well as stepped magnetization in mixed-Fe^{2+}/Fe^{3+} phosphates[11,12].

There is a large number of compounds belonging to that high-temperature polymorph α-$CrPO_4$. They are identified with the general chemical formula $\square_3M_3(XO_4)_3$ where $\square$ is a vacancy that can be filled by monovalent and/or divalent cations introducing an oxidation state decreases of the transition metal M, and XO_4 referring to tetrahedral entity respectively. They all crystallize with centrosymmetric *Imma* space group[6-24]. Interestingly, some of them with the following general formula $A_2M^{2+}{}_2M^{3+}(PO_4)_3$ where *A* is an alkali and *M* are metals able to show an oxidation equal to 2 and/or 3, were recently described as low-temperature polymorphs of the alluaudite type structure[25, 26].

, We report on the synthesis process, the crystal structure and the computational investigation of a novel mixed copper/chromium phosphate $NaCuCr_2(PO_4)_3$ (NaCuP). This work sheds light on a slight but important structural modification with respect to the *Imma* α-$CrPO_4$ type structure exemplified by $NaMCr_2(PO_4)_3$ (NaMP) (M = Co, Ni) compounds[7,10].

The *Imma* to *Imm*2 phase modification when Cu^{2+} is introduced is also supported by IR and Raman spectroscopic investigations.

2.Experimental

2.1. Synthesis

$NaCuCr_2(PO_4)_3$ (NaCuP) was prepared by conventional solid-state reaction, starting from a stoichiometric mixture of carbonate, nitrate and phosphate reactants of analytical grade Na_2CO_3, $Cu(NO_3)_2 \cdot 3H_2O$, $Cr(NO_3)_3 \cdot 9H_2O$ and $NH_4H_2PO_4$. This mixture was dissolved in aqueous acid solution, stirred continuously, then air-dried overnight in an oven at 353 K to evaporate water. The obtained dry residue was placed in a platinum crucible and heated using stepped dwell to 473 K, 673 K and 873 K for 24 hours each. . This initial heating was done in order to decompose carbonate with the emission of carbon dioxide gases, nitrate and ammonia. In a second step, the product was kept over 24 hours at 1173 K in air. During this stepped strategy, the product was quenched to room temperature with several intimately ground in an agate mortar, after each temperature step.$NaMCr_2(PO_4)_3$ (NaMP) (*M* = Co, Ni) compounds were also synthesized using the same procedure as mentioned above.

2.2. Powder X-ray diffraction measurements

The XRPD patterns of the NaMP (*M* = Co, Ni and Cu) were recorded in the angular range ($10° \leq 2\theta \leq 120°$) on a PANalitycal Bragg-Brentano type diffractometer using CuKα radiation (λ = 1.54178 Å) with a step size of 0.008° and a fixed counting time of 2 s/step.

2.3. Neutrons diffraction measurements

Neutrons diffraction data were collected in the angular range ($4° \leq 2\theta \leq 164°$) on high-resolution powder diffractometer Echidna at the OPAL research reactor (ANSTO, Lucas Height, Sidney, Australia)[27] using wavelengths of 1.6215 Å with a step size of 0.05°.

For both Powder X-ray and Neutrons diffraction collected data, a full pattern refinement was carried out by means of the Rietveld method[28] using the Fullprof program[29]. The purity of the three samples were confirmed using X-Ray and Neutrons Powder Diffraction (XRPD and NPD) as seen in the first set of figures in supporting information. To refine our structural model proposed in the manuscript, we have used a joint refinement using both RT NPD and XRPD patterns to get the reliable Cu/Cr population over the sites and

reliable oxygen position thanks to the complementary use of X-rays and neutrons in powder diffraction experiments. Individual analysis are proposed supporting information.

2.4. Electron diffraction measurements

The electron diffraction were carried using a JEOL 2100 Transmission electron microscope (TEM) operating at -200kV. The microscope is equipped with an Orius SC200D camera, able to collect electron diffraction patterns and of a double tilt specimen stage. Prior to the observation, the compound is crushed in ethanol and a drop is placed on a copper grid with a formvar carbon film.

2.5. FTIR and Raman spectroscopies

Fourier-Transform InfraRed (FTIR) and Raman spectroscopies were investigated for NaMP (M = Co, Ni, Cu) compounds. The FTIR-spectra were collected at room temperature using a Perkin Emler Paragon 1000 PC Fourier spectrometer in the range 1600–400 cm^{-1}. The measurements were performed in transmission mode. The Raman-spectra were measured in a back scattering arrangement, at room temperature, using a Horiba Jobin-Yvon Lab RAM HR 800 Dual Spectrophotometer at 50-1200 cm^{-1} with incident laser excitation 632nm.

3. Results and discussion

3.1. Structural model

Cell parameters, space group and atomic positions for the NaCoP compound were used as a starting model for the refinements of the crystal structures of the NaMP (*M*= Ni and Cu) as previously established[9]. Initially, the scale factor, two theta zero and linear interpolation type for the background were refined. Then, the profile was fitted with pseudo-Voigt profile function. In a succeeding step, the unit cell lattices and half width parameters were refined. Finally, the positional parameters, the site occupation factors and individual isotropic parameters (B_{iso}) were allowed to refine. Rietveld refinement of the powder X-ray diffraction pattern for the three compounds are shown in Figure SI.1 & 2. At this stage, when *Imma* space group is considered for the XRPD pattern, the main intensities of the peaks related to the PO_4 groups are not well superposed with calculated ones as seen in Figure SI.1a. For clarity, crystallographic planes of some of these (hkl) peaks with PO_4 groups are depicted in figure 2. Furthermore, thermal agitation factors (B_{iso}) for some crystallographic sites showed negative values in the case of NaCuP contrary to the NaCoP and NaNiP compounds.

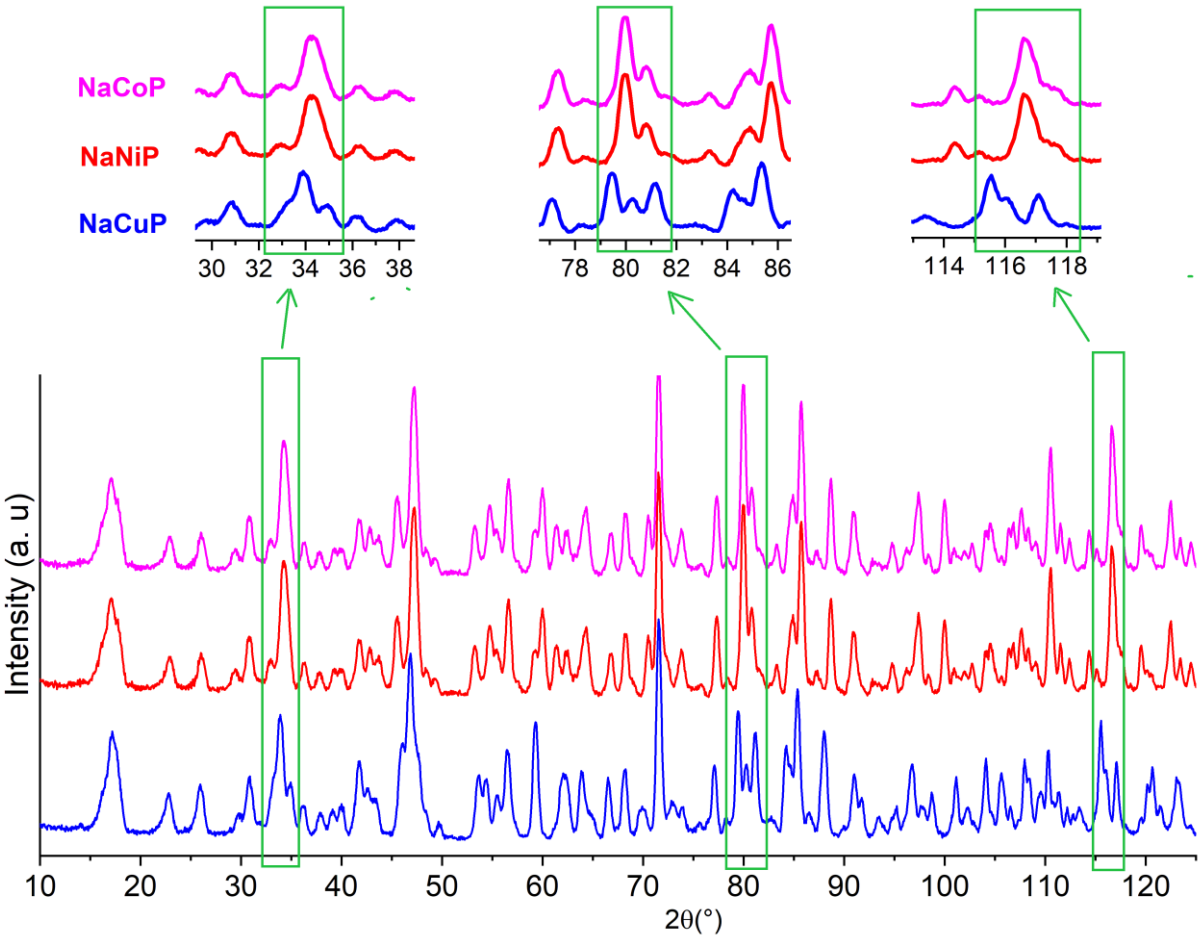

Figure 1. Superposed of observed NPD patterns recorded at room temperature for NaMP (*M* = Co (purple), Ni(red) and Cu (blue)). Enlargement of peaks around 35° and 80° and 117° given in the inset displays symmetry lowering leading to structural transition from *Imma* to *Imm*2 space groups.

In order to solve these issues, a deep analysis of NPD (Fig. 1) and XRPD (Fig. 2) patterns has been explored and leading to three interesting observations. First, the superposed NPD patterns showed peaks splitting around 35° and 80° and 117° (see enlarged parts in the top of Fig. 1). Second, in the $32° \leq 2\theta \leq 34°$ range for XRPD patterns, two unexpected behaviors were observed. The first one concerned the both (240) and (321) reflection peaks, which are well overlapped with NaMP (*M* = Co, Ni), whereas were found clearly separated with NaCuP compound (see the enlarged part in Fig. 2 and Fig. SI. 4). The second one concerned the evolution of both (240) and (202) peaks position. Indeed, the Shannon ionic radii increase from 0.69Å for Ni^{2+} to 0.72Å for Mg^{2+}, to 0.74 Å for Zn^{2+}, to 0.745 Å for Co^{2+}, resulting in a continuous evolution of both (240) and (202) peaks with the lattice parameters for

$NaMCr_2(PO_4)_3$ (*M* = Mg, Zn, Co and Ni)[7,10,15]. However, when a standard Shannon ionic radius of 0.73 Å is considered for Cu^{2+}, (202) peak positions for NaCuP clearly not support such Vegard law but rather a high contraction cell, along (010) planes, leading to symmetry lowering, induced by an expected Jahn-Teller type distortion for Cu^{2+} cations[30]. Finally, when a lowering symmetry was taken, the new peak appeared around 35° was indexed with a (hkl) reflection which is systematically absent for *Imma* symmetry (see the enlarged part in Fig. 1 and Fig. SI2c). The best results were obtained when the *Imm*2 symmetry was considered as displayed in the table SI n°1.

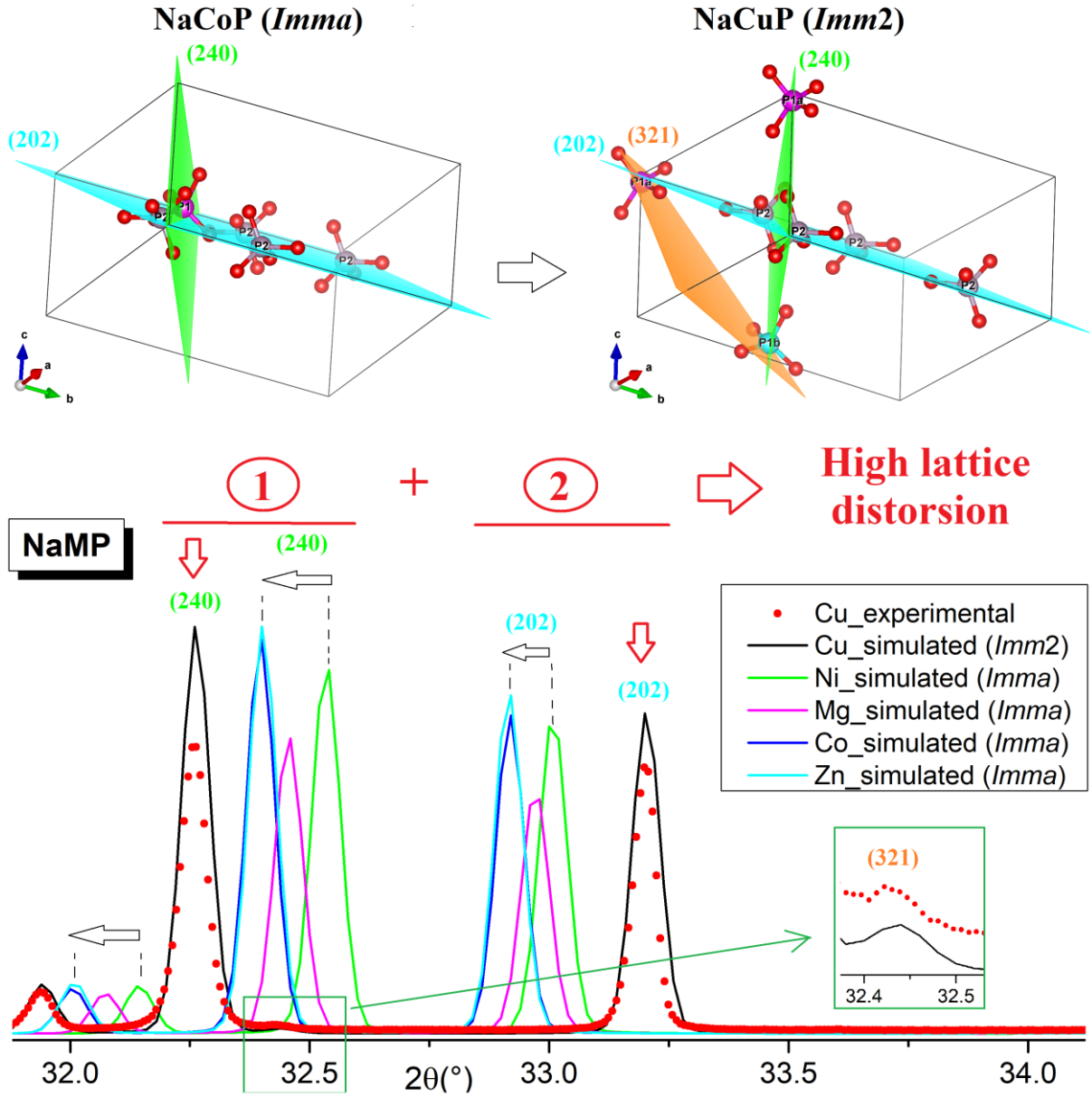

Figure 2. Superposed of observed diffraction patterns for NaCuP (crosses) with simulated diffraction patterns for $NaMCr_2(PO_4)_3$ (*M*= Mg, Zn, Co and Ni)[9,10,12] (full color lines) and simulated diffraction patterns for *Imm*2 symmetry (Full black line). The reflection planes (240), (202) and (321) and their intersection with the PO_4 tetrahedra in the two symmetries *Imma* and *Imm*2 were represented at the top of the figure.

Electron diffraction study was further performed in order to confirm the symmetry lowering from *Imma* to *Imm*2. The electron diffraction pattern obtained along the [001] zone axis show weak reflections corresponding to (110), (310) (Figure 3). The observation of these reflections, which are systematically absent for *Imma* due to a particular condition on hk0 reflections, indicates the absence of the "a" glide plane which is consistent with our analysis proposing a compound crystallizing in the *Imm*2 space group. Even if further investigations are needed to understand the weakness of the considered reflection as well as the diffusion observed on the pattern, note nevertheless that this pattern is representative of all the observed crystals.

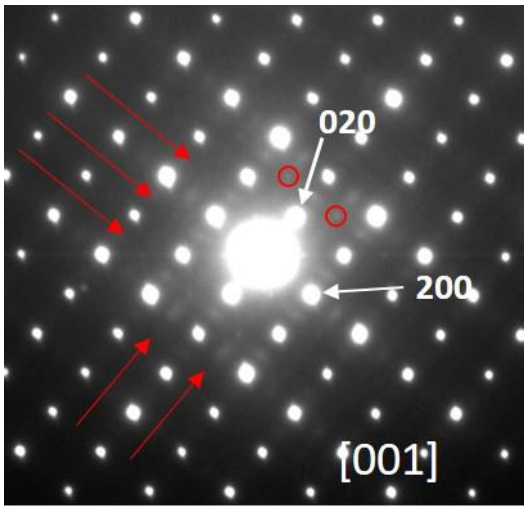

Figure 3: Representative electron diffraction pattern along the [001] zone axis. The red circles emphasis the presence of reflections forbidden in the *Imma* space group**.** The red arrows underlines the presence of diffusion

As an intermediate step of our analysis, extracted from a joint NPD-XRPD refinement, the crystal data and structure refinement parameters are presented in Table 1. Furthermore, the final refined atomic position, site occupancy and thermal parameters are given in Table 2. The final residuals (R-values) for the room temperature NPD/XRPD joint refinement are the following: R_p = 2.81%, R_B = 2.91% for XRPD pattern (3.84% for NPD pattern), χ^2 = 2.77 for $NaCuCr_2(PO_4)_3$ compounds.

Table 1. Crystal data and structure refinement parameters for NaMP (*M* = Co ; Ni and Cu) extracted from joint NPD-XRPD refinement.

Compound	**NaCoP**		**NaNiP**		**NaCuP**	
Method	**XRPD**	**NPD**	**XRPD**	**NPD**	**XRPD**	**NPD**
Chemical Formula	$NaCoCr_2(PO_4)_3$		$NaNiCr_2(PO_4)_3$		$NaCuCr_2(PO_4)_3$	
Crystal system	Orthorhombic		Orthorhombic		Orthorhombic	
Space Group	*Imma*		*Imma*		*Imm*2	
a /Å	10.411(4)		10.386(4)		10.411(1)	
b /Å	13.028(4)		12.965(8)		13.102(2)	
c /Å	6.376(1)		6.358(2)		6.302(1)	
V /Å^3	864.82(1)		856.24(1)		859.61(2)	
Z	4		4		4	
Data acquisition						
Wavelength (Å)	1.5417	1.6215	1.54178	1.6215	1.54178	1.6215
Angular range (°)	10≤2θ≤120	4≤2θ≤164	10≤2θ≤120	4≤2θ≤164	10≤2θ≤120	4≤2θ≤164
Step scan incremet	0.008°	0.05°	0.008°	0.05°	0.008°	0.05°
Structural refinement						
Program refinement	FULLPROF		FULLPROF		FULLPROF	
N. of refined parameters	46		46		71	
Continuous background	Linear interpolation		Linear interpolation		Linear interpolation	
Profile function	Pseudo-Voigt		Pseudo-Voigt		Pseudo-Voigt	
η	0.93(1)	0.20(4)	0.47(6)	0.27(5)	0.95(1)	0.25(3)
Zeropoint (2θ)	0.0178(1)°	0.3007(2)°	0.0138(1)°	0.2711(2)°	0.0327(1)°	-0.2590(9)°
N. of reflections	734/2	468	730/2	463	809/2	503
Profile settings						
U	0.021(1)	0.221(1)	0.012(4)	0.202(1)	0.033(6)	0.217(6)
V	-0.016(4)	-0.649(6)	-0.005(1)	-0.603(4)	-0.023(4)	-0.658(1)
W	0.006(1)	0.686(3)	0.005(1)	0.655(1)	0.010(7)	0.688(3)
Scale factor	$0.74(2)\times10^{-3}$	0.2589(2)	$0.73(2)\times10^{-3}$	0.4264(3)	$0.45(1)\times10^{-3}$	0.6625(2)
Asymmetryparameter	0.148(1)	0.207(1);	0.072(1);	0.136(5);	0.107(1);	0.095(1);
	0.067(4)	0.056(1)	0.039(6)	0.049(1)	0.046(8)	0.037(5)
Pref. orientation parameter	1.024(2)	0.990(6)	1.008(1)	-0.0138(1)	1.003(1)	0.976(3)
χ^2	3.04		3.88		2.77	
R_p, %	1.28	3.51	4.47	3.30	2.81	2.81
R_{wp}, %	1.87	4.43	6.19	4.23	3.65	3.55
R_{exp}, %	1.01	2.73	3.05	2.32	2.47	1.95
R_B, %	5.85	6.54	2.66	4.21	2.91	3.84
R_F, %	4.97	3.83	2.48	2.36	2.56	2.36

Table 2. Atomic coordinates and isotropic thermal displacement parameters for NaMP (*M* = Co; Ni and Cu) extracted from joint NPD-XRPD refinement.

Compounds	***Site [Wyckoff]***	***Point symmetry***	***Atom***	***X***	***Y***	***Z***	B_{iso}(Å ^{2})	***Occupancy factor***
NaCoP	X(1) [*4e*]	*mm*2	Na	0	1/4	0.4056(7)	1.660(2)	1
NaNiP	X(1) [*4e*]	*mm*2		-	-	0.4068(5)	2.880(9)	1
NaCuP	X(1a) [*2a*]	*mm*2		-	0	0.4727(1)	1.645(5)	1
	X(1b) [*2b*]	*mm*2		-	1/2	0.6611(1)	4.363(7)	1
NaCoP	M(1) [*4a*]	2/*m* . .	Cr	0	0	0	0.255(6)	1
NaNiP	M(1) [*4a*]	2/*m* . .		-	-	-	0.394(3)	1
NaCuP	M(1) [*4d*]	*m* . .		-	0.7463(7)	0.0623(1)	0.230(5)	1
NaCoP	M(2) [*8g*]	. 2 .	0.5Cr + 0.5Co	1/4	0.6334(3)	1/4	0.180(3)	0.5/0.5
NaNiP	M(2) [*8g*]	. 2 .	0.5Cr + 0.5Ni	-	0.6338(1)	-	0.601(2)	0.5/0.5
NaCuP	M(2) [*8e*]	1	0.5Cr + 0.5Cu	0.2517(8)	0.3831(2)	0.3197(1)	0.944(3)	0.5/0.5
			P					
NaCoP	P(1) [*4e*]	*mm*2		0	1/4	0.9163(5)	0.259(7)	1
NaNiP	P(1) [*4e*]	*mm*2		-	-	0.9197(3)	0.275(4)	1
NaCuP	P(1a) [*2a*]	*mm*2		-	0	0.0013(1)	1.137(3)	1
	P(1b) [*2b*]	*mm*2		-	1/2	0.1632(2)	0.209(3)	1
			P					
NaCoP	P(2) [*8g*]	. 2 .		1/4	0.4254(1)	1/4	0.157(5)	1
NaNiP	P(2) [*8g*]	. 2 .		-	0.4262(4)	-	0.346(3)	1
NaCuP	P(2) [*8e*]	1		0.2521(1)	0.1765(2)	0.3224(1)	0.408(4)	1
			O					
NaCoP	O(1) [*8h*]	*m* . .		0	0.6530(4)	0.9486(7)	0.379(7)	1
NaNiP	O(1) [*8h*]	*m* . .		-	0.6528(1)	0.9484(4)	0.298(4)	1
NaCuP	O(1a) [*4d1*]	*m* . .		-	0.4057(9)	0.0147(4)	1.371(3)	1
	O(1b)[*4d2*]	*m* . .		-	0.0983(9)	0.1158(2)	0.946(2)	1
			O					
NaCoP	O(2) [*8i*]	. *m* .		0.8823(3)	1/4	0.7672(6)	0.712(7)	1
NaNiP	O(2) [*8i*]	. *m* .		0.8806(2)	-	0.7714(1)	0.316(4)	1
NaCuP	O(2a) [*4c1*]	. *m* .		0.3843(2)	0	0.8040(2)	2.099(3)	1
	O(2b) [*4c2*]	. *m* .		0.6192(2)	1/2	0.3366(5)	0.311(2)	1
			O					
NaCoP	O(3) [*16j*]	1		0.2143(1)	0.3637(2)	0.4372(3)	0.402(4)	1
NaNiP	O(3) [*16j*]	1		0.2164(3)	0.3631(1)	0.4394(2)	0.493(2)	1
NaCuP	O(3a) [*8e1*]	1		0.2228(6)	0.1160(5)	0.5107(2)	0.118(9)	1
	O(3b) [*8e2*]	1		0.7875(7)	0.3897(6)	0.6261(1)	0.869(2)	1
			O					
NaCoP	O(4) [*16j*]	1		0.1370(2)	0.5064(1)	0.2131(3)	0.474(4)	1
NaNiP	O(4) [*16j*]	1		0.1391(5)	0.5080(1)	0.2113(2)	0.432(3)	1
NaCuP	O(4a) [*8e1*]	1		0.1340(8)	0.2522(6)	0.2781(2)	1.159(1)	1
	O(4b) [*8e2*]	1		0.8598(7)	0.2408(5)	0.8559(1)	0.226(2)	1

3.2 Structural description

The structural description is mainly limited to the specific change observed in NaCuP that is close to those previously reported for $Na_{1+x}Mg_{1+x}Cr_{2-x}(PO_4)_3$ (x = 0; 0.2)[15] and

$NaZnCr_2(PO_4)_3$[15], $NaCoCr_2(PO_4)_3$[10], $NaNiCr_2(PO_4)_3$[7] and crystallizing with the known α-$CrPO_4$ structure. Changes from *Imma* to *Imm*2 space group are illustrated in Figure 4 and sum up in Table 2. Both the C_2 rotation axis and the plan elements passing through M(2) and P(2) crystallographic sites are suppressed. It can be noticed that P(1), Na and O(n) sites can be splitted into P(1a) & P(1b) ; Na(1a) & Na(1b) and O(na) & O(nb) (1 < n < 4), respectively. From a terminological viewpoint, the term "phase change" is better used than "phase transition" because one did not study any stimulus dependence as temperature in $LiSn_2(PO_4)_3$[31]. The solid solution $NaCu_{1-x}Co_xCr_2(PO_4)_3$ or $NaCu_{1-x}Ni_xCr_2(PO_4)_3$ as not being studied yet to evidence for which x values the *Imma* space group is stable with respect to *Imm*2.

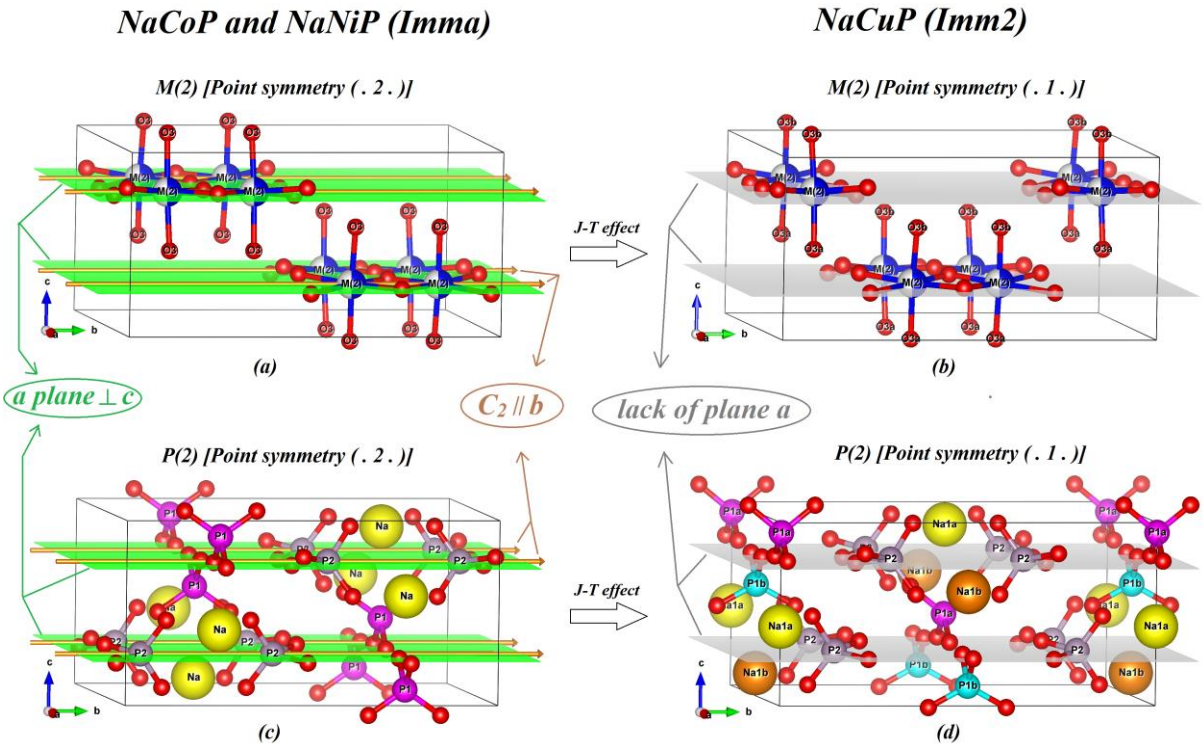

Figure 4. *Imma* to *Imm*2 phase change on the α-$CrPO_4$ lattice type in NaCuP (b, d), showing the suppression of C_2 rotation axis and a plane symmetry elements passing through M(2) and P(2) crystallographic sites (a, c).

The projected NaCuP structure along a & b crystallographic directions is shown in Figure 5. This representation is similar to the previous ones reported with an open character of the 3D framework forming intersecting tunnels where the Na^+ countercations are located. The framework can be described by a 3D assemblage of PO_4 tetrahedra, $Cr(1)O_6$ and $M(2)O_6$ (M(2) = 0.5Cu + 0.5Cr) octahedra. The $M(2)O_6$ octahedra share an edge to form $M_2(2)O_{10}$ dimer units. The dimer units share corners and edges with PO_4 tetrahedra to form sheets in the

(100) plane. The sheets are interconnected through the $[CrPO_8]^{8-}$ infinite chain (figure 6) to form the 3D-framwork of NaCuP. Such sheets are linked along (100) direction through the infinite chains $[CrPO_8]^{8-}$ leading to $[CuCr_2(PO_4)_3]_\infty$ 3D framework (see Figure 7).

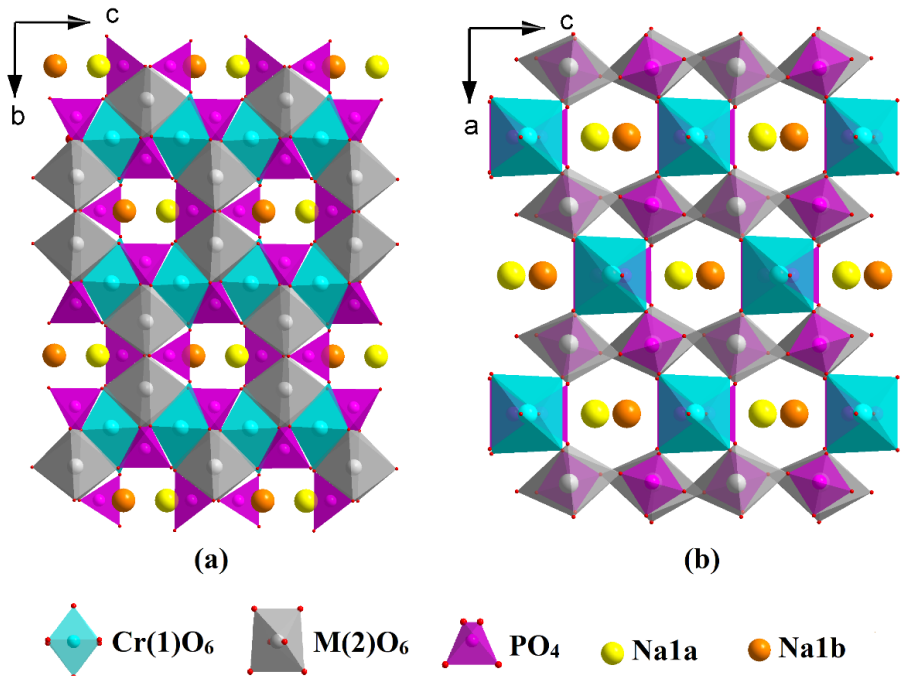

Figure 5. Projections along the a-axis (a), b-axis (b) of the structure of $NaCuCr_2(PO_4)_3$, showing the intersecting tunnels in which the Na^+ countercations are located.

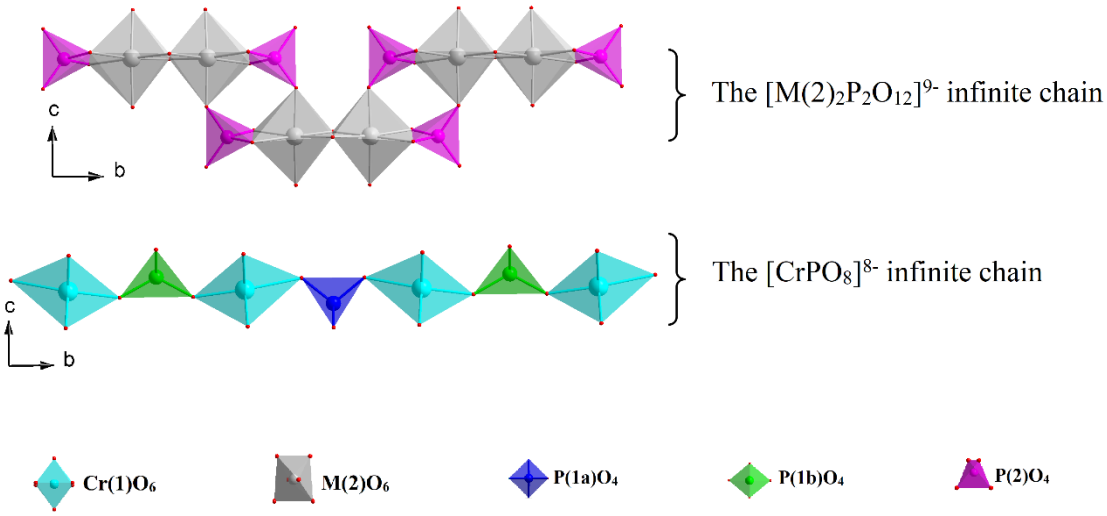

Figure 6. Views of the two infinite chains parallel to b-axis: chains of corner-sharing $Cr(1)O_6$ octahedra- PO_4 tetrahedra and those of edge-sharing $[M(2)O_6]$ octahedra linked by PO_4 tetrahedra in $NaCuCr_2(PO_4)_3$.

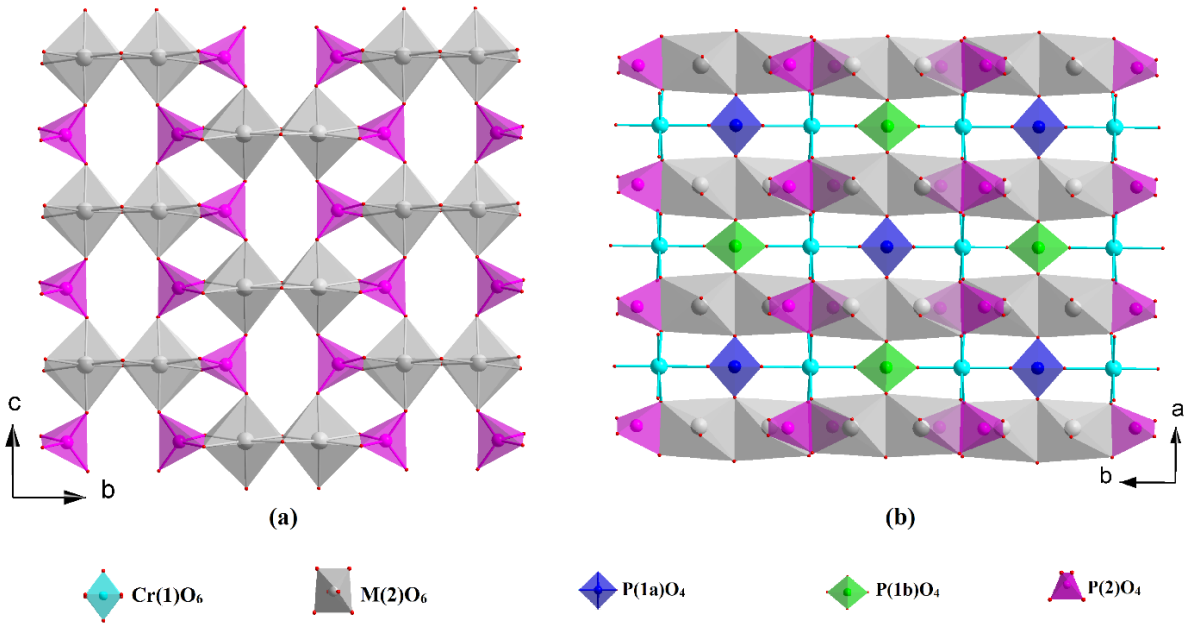

Figure 7. (a) Sheets of edge and corner-sharing $M(2)_2O_{10}$ units and PO_4 tetrahedra along (100) ; (b) Association of sheets by infinite chains $[CrPO_8]^{8-}$ leading to $[CuCr_2(PO_4)_3]_\infty$ framework.

The structural models for the three Na*M*P componds (*M* = Co, Ni and Cu) were also validated by Bond Valence Shell (BVS) and CHARDI calculations that are reported on Table 3. For the BVS method, from the observed bond lengths (R_{ij}) and BV parameter b and R_o given by Gagne & Hawthorne[31], the valences of the individual bonds Sij, were calculated, using the procedure described by Brown & Altermatt[32].

Table 3. CHARDI and BVS calculations of the cation polyhedral in three compounds NaMP (*M* = Co, Ni, Cu).

Site(i)		**CN(i) coordination number**	**ECoN(i) effective coordination number**			**q(i) formal oxidation number**			**V(i).sof(i) computed valence * site occupation factor**			**Q(i) computed charges**			**q(i)/Q(i)**		
Na1	Na1a	8	7.92	7.92	7.61	1.00	1.00	1.00	0.84	0.83	0.77	0.98	0.99	0.96	1.02	1.01	1.04
	Na1b				7.88			1.00			0.94			1.05			0.96
Cr1		6	5.97	5.99	5.88	3.00	3.00	3.00	2.90	2.91	2.97	3.15	3.04	3.13	0.95	0.99	0.96
M2 = 0.5Cr + 0.5 M		6	*Co*	*Ni*	*Cu*	*Co*	*Ni*	*Cu*	*Co*	*Ni*	*Cu*	*Co*	*Ni*	*Cu*	*Co*	*Ni*	*Cu*
			6.00	5.99	5.85	2.50	2.50	2.50	2.45	2.51	2.42	2.46	2.48	2.46	1.02	1.01	1.02
P1	P1a	4	3.99	3.97	3.80	5.00	5.00	5.00	4.94	4.99	4.90	4.99	4.97	4.98	1.00	1.01	1.00
	P1b				3.94			5.00			5.15			5.11			0.98
P2		4	3.81	3.89	3.83	5.00	5.00	5.00	4.96	4.96	4.95	4.98	5.02	4.95	1.00	1.00	1.01

Let us note that this model is based on the convention that only the nearest neighbors contribute to the BVS. The postulate that the BVS surrounding the i^{th} ion is equal to the oxidation state V_i, as shown in equation (2), has been checked for these 3 compounds.

$$S_{ij} = exp\left[\frac{R_0 - R_{ij}}{b}\right] \quad (1)$$

$$V_i = \sum_j S_{ij} \quad (2)$$

The second validation tool, i.e. the CHARDI method, exploits only the experimental bond lengths to compute the effective coordination number (ECoN) (a non-integer coordination number) and distributes the formal oxidation number weighted by the site-occupation factor (q) of each atom among all its bonds as a function of the ECoN. By labelling Q the computed charges, the q/Q ratio for the cations is the internal criterion for such an evaluation[34]. This model has been successfully used to validate numerous crystal structures[25-26,35-37]. The convergence of the result is evaluated by the mean absolute percentage deviation (MAPD), which measures the agreement between Q and q for the complete sets of the polyhedron-centering atoms and the vertex (corner) atoms. The MAPD parameter was calculated using equation (3)[38]:

$$MAPD = \frac{100}{N}\sum_{i=1}^{N}\left|\frac{q(i) - Q(i)}{q(i)}\right| \quad (3)$$

Where N is the number of polyhedron-centering or vertex atoms in the asymmetric unit. The CHARDI computations were carried out with the CHARDI2015 Fortran program[39-40] and summed up in Table 3 with BVS calculations outputs.

Table 4. Distortion Index of d(M(1 & 2)-O) distances in NaMP (*M* = Co, Ni, Cu) compounds.

Compounds	NaCoP	NaNiP	NaCuP
DI (M(2)-O) with M(2) = 0.5M + 0.5Cr	0.42%	0.51%	2.38%
DI (Cr(1)-O)	1.09%	0.72%	2.06%

Even if CHARDI and BVS calculations confirm that the formal oxidation number/ computed charges ratios (q(i)/Q(i)) converge towards 1 in NaMP (M= Co, Ni and Cu) validating our approach, refined main interatomic distances were also finely considered to support the symmetry lowering. First, a significant distortion index is shown for both octahedral environments in NaCuP regarding NaMP (M = Co, Ni) as reported in Table 4. The *Imma* to *Imm*2 symmetry lowering can be likely assigned to a Jahn-Teller distortion in $Cu^{2+}O_6$ and $Cr^{2+}O_6$ octahedra. A charge compensation equilibrium $Cu^{2+} + Cr^{3+} \leftrightarrow Cu^{3+} + Cr^{2+}$ with an

hoping mechanism from one to another transition metal crystallographic site through O(4a) and/or O(4b) need then to be considered.

Table 5. Selected interatomic distances (Å) and in NaCoP, NaNiP and NaCuP extracted from the joint X-Ray & Neutron powder Diffraction.

	NaCoP	**NaNiP**	**NaCuP**	
	XRPD & NPD	**XRPD & NPD**	**XRPD & NPD**	
Cr(1)-O(4) × 4	1.971(5)	1.976(1)	Cr(1)-O(4a) × 2	1.967(1)
Cr(1)-O(1) × 2	2.020(5)	2.008(1)	Cr(1)-O(4b) × 2	1.936(1)
			Cr(1)-O(1a) × 1	2.016(1)
			Cr(1)-O(1b) × 1	2.071(1)
<Cr(1)-O>	**1.987**	**1.987**	**<Cr(1)-O>**	**1.982**
M(2)-O(3) × 2	2.029(2)	2.006(1)	M(2)-O(3a) × 1	1.972(1)
M(2)-O(4) × 2	2.044(1)	2.012(1)	M(2)-O(3b) × 1	1.998(1)
M(2)-O(2) × 2	2.053(3)	2.032(1)	M(2)-O(4a) × 1	2.123(1)
			M(2)-O(4b) × 1	1.992(1)
			M(2)-O(2a) × 1	2.089(3)
			M(2)-O(2b) × 1	2.041(3)
<M(2)-O>	**2.042**	**2.017**	**<M(2)-O>**	**2.036**
P(1)-O(1) × 2	1.529(1)	1.514(1)	P(1a)-O(1b) × 2	1.493(5)
P(1)-O(2) × 2	1.551(1)	1.558(1)	P(1a)-O(2b) × 2	1.599(1)
<P(1)-O>	**1.540**	**1.536**	**<P(1a)-O>**	**1.546**
			P(1b)-O(1a) × 2	1.556(1)
			P(1b)-O(2a) × 2	1.493(1)
			<P(1b)-O>	**1.525**
P(2)-O(3) × 2	1.486(2)	1.498(1)	P(2)-O(3a) × 1	1.467(5)
P(2)-O(4) × 2	1.599(1)	1.584(1)	P(2)-O(3b) × 1	1.524(1)
			P(2)-O(4a) × 1	1.599(4)
			P(2)-O(4b) × 1	1.579(2)
<P(2)-O>	**1.543**	**1.541**	**<P(2)-O>**	**1.542**
Na(1)-O(1) ×2	2.588(4)	2.587(1)	Na(1a)-O(1b) × 2	2.554(2)
Na(1)-O(2) ×2	2.610(5)	2.629(1)	Na(1a)-O(2b) × 2	2.641(4)
Na(1)-O(3) ×4	2.685(5)	2.692(1)	Na(1a)-O(3a) × 4	2.785(3)
<Na(1)-O>	**2.642**	**2.650**	**<Na(1a)-O>**	**2.691**
			Na(1b)-O(1a) × 2	2.528(2)
			Na(1b)-O(2a) × 2	2.569(1)
			Na(1b)-O(3b) × 4	2.649(2)
			<Na(1b)-O>	**2.599**

Secondly, as expected for a monophosphate[41], all P-O distances have an overall value of 1.537 Å (Table 5) and PO_4 distortion indexes are lower than 5.4% (table 6). However, all

coordination polyhedra P(i)O_4 are strongly distorted in NaCuP in opposite to NaMP (M = Co and Ni) phosphates. Consequently, the infinite chain $[Cr(1)PO_8]^{8-}$ priory illustrated in Fig. 6 shows a kind of breathing mode with an alternative sequence of highly distorted P(1a)O_4 and less distorted P(1b)O_4 with respect to NaMP (M= Co, Ni). This phenomenon is in contrast with the $[M(2)_2P_2O_{12}]^{9-}$ with M2 = 0.5 Cr + 0.5 Cu infinite chain for which the involved P(2)O_4 polyhedra are in average slightly modified. If one focuses on the P(1a)O_4 and P(1b)O_4 polyhedra, both show a distortion index of d(P-O) distances relatively higher in NaCuP than those in NaMP (M= Co Ni). Whereas the two shorter distances become shorter when the two larger becoming larger in P(1a)O_4, the tendency is reversed in P(1b)O_4 with the shorter becoming the larger ones and vice versa. It results then in a second kind of breathing mode type between P(1b)-O(2a)-M(2) occurring perpendicular to the $[M(2)_2P_2O_{12}]^{9-}$ infinite chains. That is why, the consideration of $Cu^{2+}O_6$ and $Cr^{2+}O_6$ Jahn-Teller octahedra would also be indirectly supported by an enhancement of the distortion index of d(P(1a & b)-O) distances.

Table 6. Distortion Index of d(P-O) distances in NaMP (M = Co, Ni, Cu) compounds.

Compounds	NaMgP*	NaZnP*	NaCoP	NaNiP	NaCuP
DI (P(1a)-O) [4e]	0.91%	0.81%	0.71%	1.43%	3.43%
DI (P(1b)-O) [4e]	0.91%	0.81%	0.71%	1.43%	2.06%
DI (P(2)-O) [8g]	2.75%	2.31%	3.66	2.79%	3.03%

* d(P-O) distances given by[15]

In addition, contrary to NaMP (*M*= Co, Ni) where sodium occupies a single type of site, the Na^+ ions in NaCuP are distributed over two distinct sites within the tunnels, namely Na(1a) and Na(1b) (Fig. 8). The polyhedral coordination was determined assuming cation-oxygen distances below the limit L_{max} = 3.13 Å, suggested by Donnay and Allman[42]. However, none of the considered Na-O distances are higher than the one's proposed for Na(1a)-O(3a) equal to 2.785 Å (see table n°5) allowing us not to consider possible Na...O interactions within our polyhedral. Polyhedral coordination does not change in number with the space group modification: still consisting of eight oxygen atoms with Na(1a)-O distances between 2.554(2) Å and 2.785(3) Å and Na(1b)-O distances between 2.528(2) Å and 2.649(2) Å (see Table 5). Interestingly, it is the polyhedral size that is impacted giving two different channel sizes with one larger and the other's smaller than the one's depicted for NaMP (*M*= Co, Ni).

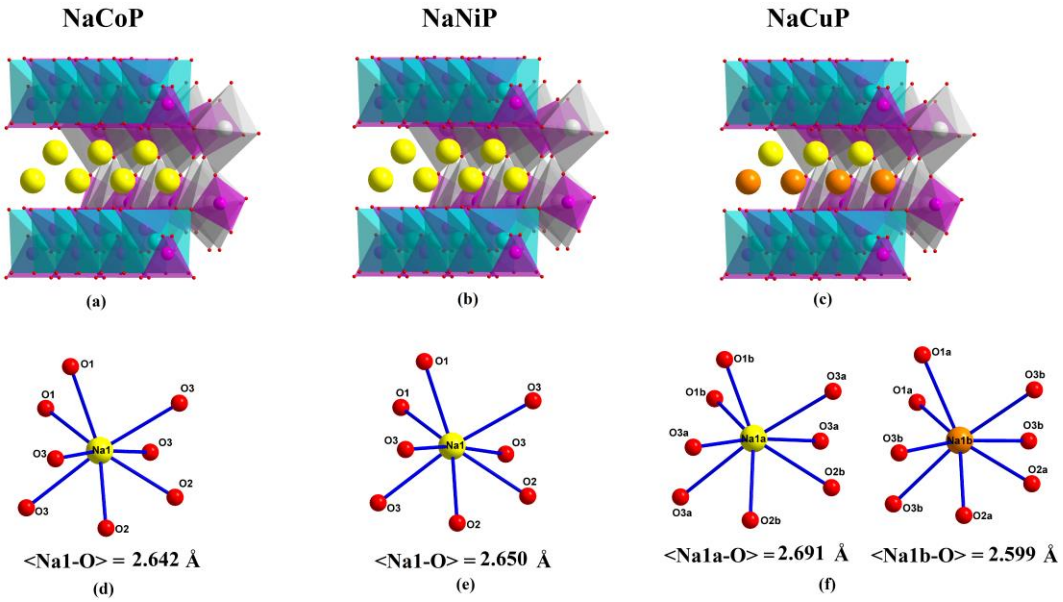

Figure 8. The oxygen environments of the sodium atoms in NaMP (M= Co, Ni and Cu).

3.2. IR spectroscopy

Infrared absorption spectra were recorded in order to examine the presence of monophosphate groups[43,44]. Figure 9 shows spectra measured for the three compounds NaCoP, NaNiP and NaCuP. The attribution of the observed bands to corresponding vibrational modes was performed on the basis of previous studies on phosphates[45,46]. The observed bands in the wave-number ranges 1275-1020 cm^{-1} and 1020-822 cm^{-1} are attributed to asymmetric (ν_3) and symmetric P-O stretching (ν_1), respectively. The bands observed between 712 and 400 cm^{-1} can be assigned to both asymmetric (ν_4) and symmetric (ν_2) of O-P-O bending, and the stretching vibrations of the MO_6 octahedra. Interestingly, the observed bands at 1020-822 cm^{-1} show the same bands vibrations type (ν_1) for NaCoP and NaNiP compounds assigned to both symmetric stretching vibration P(1)-O and P(2)-O of the two distinct crystallographic tetrahedral $P(1)O_4$ and $P(2)O_4$. This observation is in good agreement with previous studies of $NaM^{II}Cr_2(PO_4)_3$ (M^{II} = Zn, Mg)[15]. However, broader bands and less intense are observed at 1020-822 cm^{-1} for the NaCuP compound. These measurements could supported our structural analysis predicting three distinct types of crystallographic tetrahedra $P(1a)O_4$, $P(1b)O_4$ and $P(2)O_4$ and then resulting in a P-O stretching mode redistribution with the symmetry lowering. However, a precise assignment is complicated[47] and a group theoretical analysis would be necessary. Indeed, the internal mode splitting might be a consequence of a change in the site-symmetry as one proposed as well as correlation effect[48].

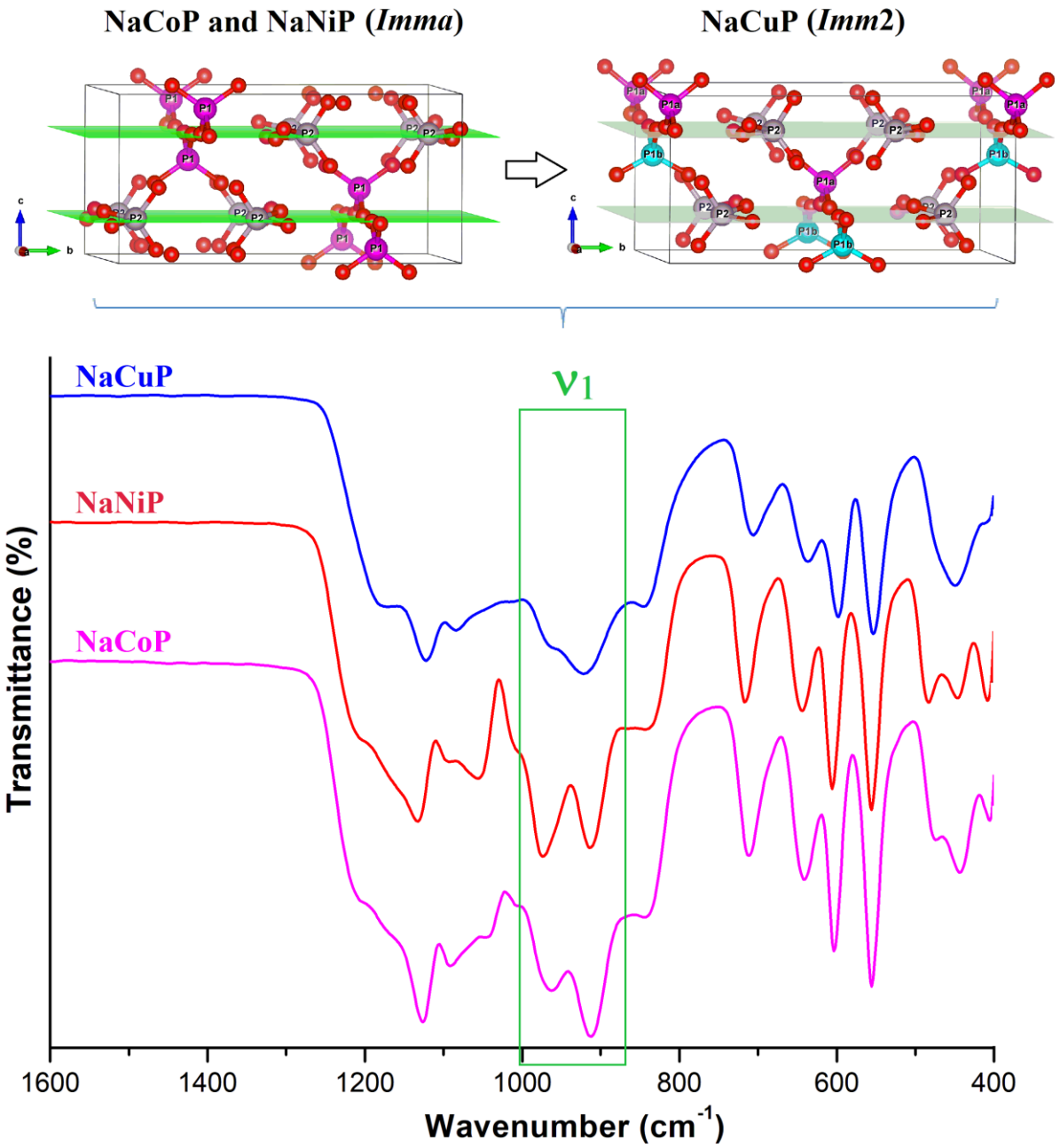

Figure 9. Top: The subdivision of P(1) site into two distinct crystallographic sites P(1a) and P(1b) deduced from lowering of symmetry. Bottom: IR spectra of NaCoP, NaNiP and NaCuP. the green rectangle shows (ν_1) vibration changes

3.3. Raman spectroscopy

In order to further consolidate our structural analysis, Raman spectroscopy for the three compounds NaMP (*M*= Co, Ni and Cu) were also carried out at room temperature. As known the scattered Raman intensity is obtained after division by the Bose–Einstein population factor $n(\omega)+1$ associated with the first - order Stokes scattering with $n(\omega) = \left(e^{\hbar\omega/KT} - 1\right)^{-1}$ [49]. This correction is obviously significant and necessary for high temperature and low wavenumber where it allows discarding additional bands as artifacts within the fitting process[50]. In our case, this correction have been applied for the three compounds NaMP (M= Co, Ni and Cu) to extract the scattered Raman intensity contributions as shown in Figure 10. A high enhancement of the scattered intensity observed at wavenumber around 100cm^{-1} for NaCuP is shown with respect to the corrected spectra of NaMP (M= Co, Ni) (Figure 10d).

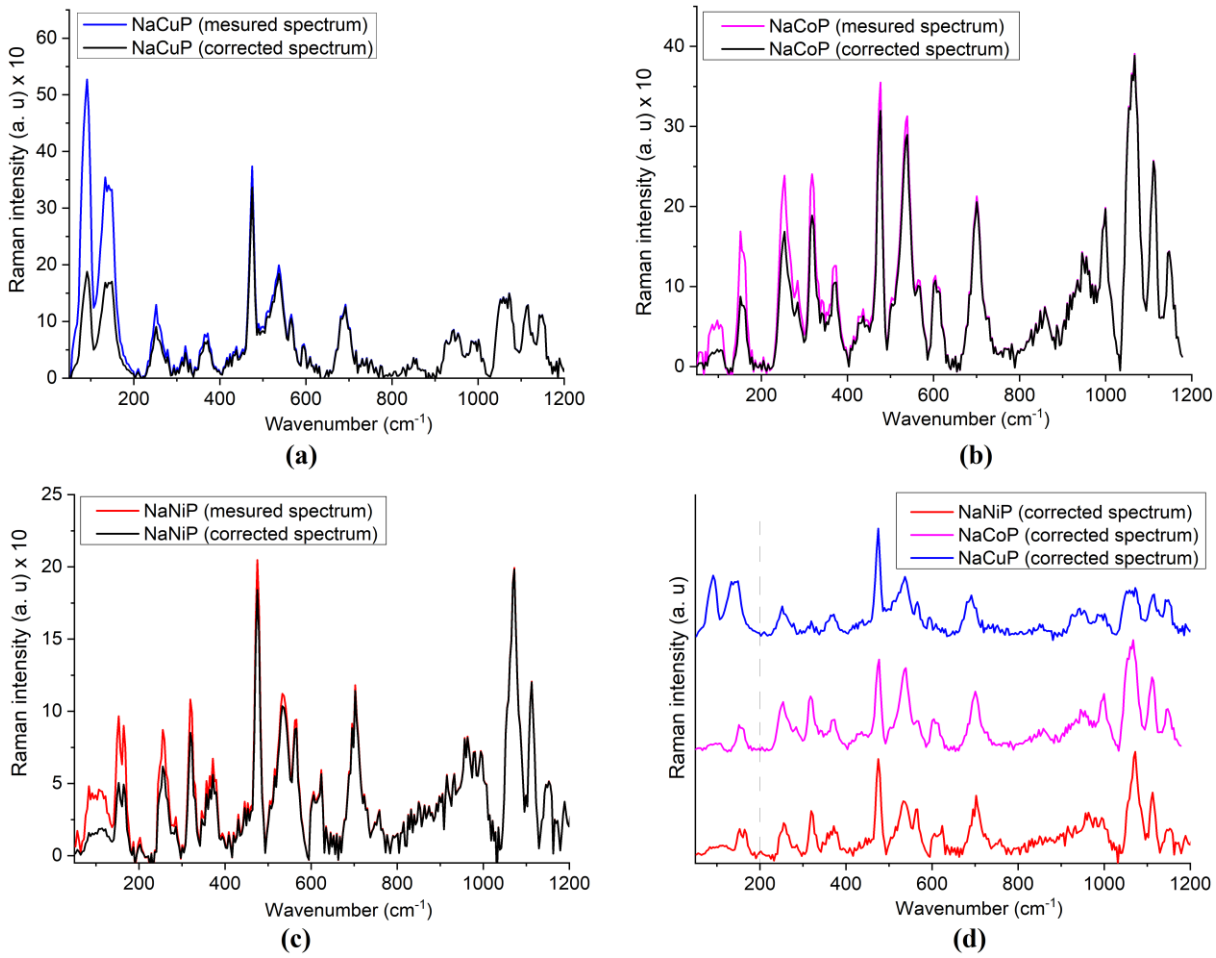

Figure 10. Measured and Corrected Raman spectra of NaMP (*M* = Cu (a); Co (b) and Ni(c)) compounds at a 298 K and corrected ones (d). Corrected spectra are obtained after dividing the measured ones by the Bose–Einstein population factor.

Having in mind that optical phonon due to lattice vibrations can be detected in the low wavenumber range, the scattered intensity enhancement shown by NaCuP supports the lattice symmetry lowering. It would especially suggests a strong coupling effect between phonon and electronic continuum[51] as already been proposed for interpreting fine structure between 70 and 140 cm^{-1} for mixed Cu^{3+}/Cu^{2+} oxidation states[52,53]. That is why, even if data collection on single crystal allowing to perform polarization analysis would be better, the present Raman spectroscopy study corroborate the charge transfer $Cu^{2+} + Cr^{3+} \leftrightarrow Cu^{3+} + Cr^{2+}$ previously pointed out from joint XRPD and NPD study.

3.4. Deformation density

Among chemical feedbacks that can be deduced from density deformation studies, the effective charge on each atom and experimental determination of the population of the d orbitals are very interesting parameters[54,55]. Especially, Sakai et al.[56] have demonstrated the possibilities to obtain theoretical deformation maps for 5d compounds, which is quite similar to the experimental results reported by Takazawa *et al*.[57]. Indeed, the experimental d electrons distribution gives 1.9(7) for the e_g orbital population and 6.14(8) for the t_{2g} close to the theoretical values are 1.90 and 5.93 respectively[56,57]. The joint XRPD and NPD analysis highlights higher distortion indexes values in the two type of transition metal polyhedra than those calculated in NaMP (*M*= Co, Ni). In order to study the spatial distribution of the electrons involved in the chemical bonding in our noncentrosymetric phosphate, 3D deformation density for the dimer $CrCuO_{10}$ surrounded by the four next neighbor CrO_6 octahedral has been plotted over the electron density iso-surface (with 0.008 $e.au^{-3}$) using Crystal Explorer 17.5[58] and the TONTO system[59,60]. As starting point, ab initio wave functions were obtained from a Hartree-Fock approximation in the 6-31G(d-p) basis sets. Figure 11 shows the distribution of charge depletion (CD) region in red color and charge concentration (CC) region in blue color on each atom in M_2O_{10} dimer with their environment octahedral CrO_6 at the crystal geometry respectively. Interestingly, a large region of charge concentration (CC) was observed on both O(4a) and O(4b) oxygens, which could not be observed on the others oxygen of the cluster dimmer-octahedral (Figure 11). This behavior could be explained by polaron Jahn-Teller formation suggested by the high distortion shown in MO_6 polyhedral containing Cu^{2+} and/or Cr^{2+}[30]. The hopping from one to another transition metal crystallographic site would occurs through both O(4a) and O(4b) oxygen definitively.

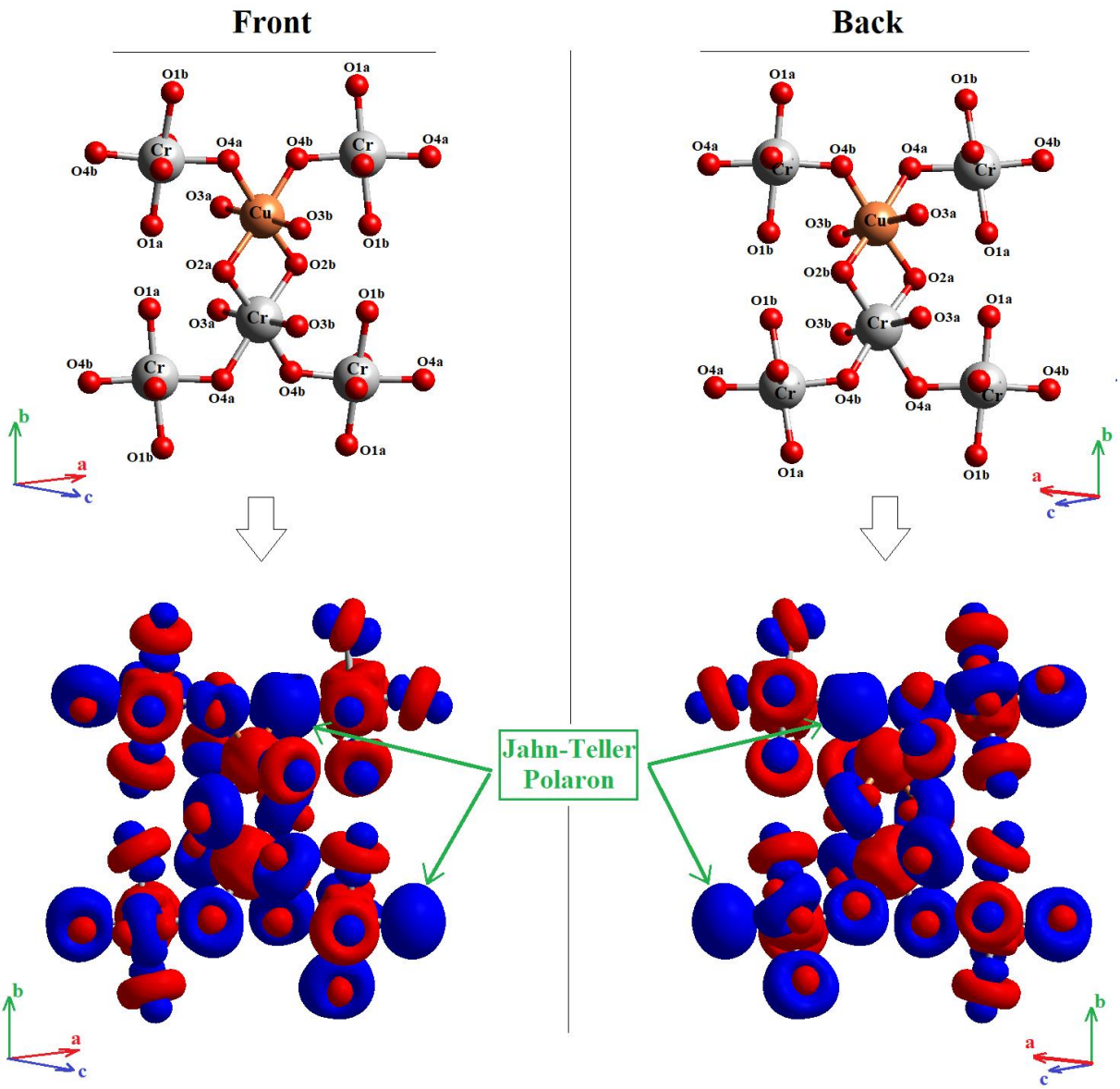

Figure 11 : D-deformation density map showing the presence of CD regions (in red) and CC regions (in blue) on the $CrCuO_{10}$ units with their environment octahedral CrO_6 leading to evidence Jahn-Teller polaron formation as observed on O(4a/b) oxygens. The isosurfaces are drawn at 0.008 e/au^{-3}.

4. Conclusion

A mixed copper/chromium phosphate $NaCuCr_2(PO_4)_3$, related to the known α-CrPO4 type structure, has been synthesized using high temperature solid state reaction and thoroughly structurally explored by an electron and combining X-rays and neutron powder diffraction, Fourier transform infrared and Raman spectroscopies. Our study shows the first phosphate belonging to the α-$CrPO_4$ type and crystallizing in the noncentrosymmetrical space group *Imm*2. The occurrence of charge compensation equilibrium $Cu^{2+} + Cr^{3+} \leftrightarrow Cu^{3+} + Cr^{2+}$

with a hopping phenomenon from one to another transition metal crystallographic site through O(4a/b) is proposed as a key factor to the centro *Imma* to noncentro-symetric *Imm*2 phase change as suggested by deformation density approach and Raman spectroscopy. Our work proposes that a new phosphates family can be explored starting from α-$CrPO_4$ type framework and introducing Jahn-Teller cations to reach optical activity, pyroelectricity and/or piezoelectricity properties with single crystal growth.

References

[1] Delmas, C.; Maccario, M.; Croguennec, L.; Le Cras, F.; Weill, F. Lithium deintercalation in $LiFePO_4$ nanoparticles via a domino-cascade model, *Nat. Mater*. **2008**, 7, 665–671.

[2] Franger, S.; Le Cras, F.; Bourbon, C.; Rouault, H. $LiFePO_4$ synthesis routes for enhanced electrochemical performance, Electrochem. *Solid-State Lett*. **2002**, 5, A231–A233.

[3] Kubota, K.; Komaba, S. Review-Practical Issues and Future Perspective for Na-Ion Batteries. *J. Electrochem. Soc*. **2015**, 162 (14), A2538-A2550.

[4] Wang, L. P.; Yu, L.; Wang, K.; Srinivasan, M.; Xu, Z. J. J. Recent developments in electrode materials for sodium-ion batteries. *J. Mater. Chem. A* **2015**, 3, 9353-9378.

[5] Huang, L.; Cheng, J.; Li, X.; Wang, B. Electrode Nanomaterials for Room Temperature Sodium-Ion Batteries: A Review. *J. Nanosci. Nanotechnol*. **2015**, 15, 6295-6307.

[6] Song, J.; Wang, K.; Zheng, J.; Engelhard, M. H.; Xiao, B.; Hu, E.; Zhu, Z.; Wang, C.; Sui, M.; Lin, Y. Controlling Surface Phase Transition and Chemical Reactivity of O3-Layered Metal Oxide Cathodes for High-Performance Na-ion Batteries. *ACS Energy Lett.* **2020**, *5*, 1718– 1725,

[7] Ben Yahia, H.; Essehli, R.; Avdeev, M.; Park, J-B.; Sun, Y-K.; Al-Maadeed, M. A.; Belharouak, I. Neutron diffraction studies of the Na-ion battery electrode materials $NaCoCr_2(PO_4)_3$, $NaNiCr_2(PO_4)_3$, and $Na_2Ni_2Cr(PO_4)_3$ *J. Solid State Chem*., **2016**, 238, 103-108.

[8] Alkhateeb A. and Ben Yahia H. Investigation of the Inorganic Compounds $NaMV_2(PO_4)_3$ (M = Fe, Co, Ni) as Anode Materials for Sodium-Ion Batteries. *ACS Omega* **2020**, 5, 30799−30807

[9] Kunomura, N.; Matsui, N.; Kumada, N.; Muto, F. Synthesis and crystal structure of $NaV_3P_3O_{12}$: A stuffed structure of α-$CrPO_4$ *J. Solid State Chem.,* **1989**, 79, 232-237.

[10] Souiwa, K.; Chennabasappa, M.; Decourt, R.; Amara, M. B.; Hidouri, M.; Toulemonde, O. Novel Mixed Cobalt/Chromium Phosphate $NaCoCr_2(PO_4)_3$ Showing Spin-Flop Transition *Inorg. Chem.,* **2015** 54 7345-7352.

[11] Shang, M. Y.; Chen, Y.; Tian, G., Yuan, H. M.; Feng, S. H. Re-entrant spin glass and stepped magnetization in mixed-valence $SrFe_3(PO_4)_3$ *J. Phys. B,* **2013**, 409, 42-46.

[12] David, R.; Pautrat, A.; Kabbour, H.; Mentré, O. Common Building Motifs in $Ba_2Fe_3(PO_4)_4{\cdot}2H_2O$, $BaFe_3(PO_4)_3$, and $Na_3Fe_3(PO_4)_4$: Labile Fe^{2+}/Fe^{3+} Ordering and Charge-Dependent Magnetism *Inorg. Chem.,* **2016**, 55, 4354-4361.

[13] Attfield, J. P.; Cheetham, A. K.; Cox, D. E.; Sleight, A. W. Synchrotron X-ray and neutron powder diffraction studies of the structure of α-CrPO4, *J. Appl. Cryst.* **1988**, 21, 452-457.
[14] Rittneret, P.; Glaum, R. Kristallzüchtung und Einkristallstrukturverfeinerungen der Rhodium(III)-phosphate $RhPO_4$ und RhP_3O_9, *Z. Anorg. Allg. Chem.*, **1994**, 209, 162-169.
[15] Souiwa, K.; Hidouri, M.; Toulemonde, O.; Duttine, M.; Amara, M. B. Synthesis and characterization of the phosphates $Na_{1+x}Mg_{1+x}Cr_{2x}(PO_4)_3$ (x = 0; 0.2) and $NaZnCr_2(PO_4)_3$ with the α-CrPO4 structure *J. Alloys Compd.* **2015**, 627, 153−160.
[16] Korzenski, M. B.; Kolis, J. W.; Long, G. J. Hydrothermal Synthesis, Structural Characterization, and Physical Properties of a New Mixed Valence Iron Phosphate, $SrFe_3(PO_4)_3$, *J. Solid State Chem.*, **1999**, 147, 390-398.
[17] Ouaatta, S.; Assani, A.; Saadi, M.; Ammari, L. El. Crystal structure of strontium dinickel iron orthophosphate *Acta Cryst.*, **2015**, E71, 1255-1258.
[18] Bouraima, A.; Makani, T.; Assani, A.; Saadi, M.; Ammari, L. El. Crystal structure of strontium dicobalt iron(III) tris(orthophosphate): $SrCo_2Fe(PO_4)_3$ *Acta Cryst.*, **2016**, E72, 1143-1146.
[19] Alhakmi, G.; Assani, A.; Saadi, M.; Follet, C.; Ammari, L. E. $SrMn^{II}_2Mn^{III}(PO_4)_3$. *Acta Cryst*., **2013**, E69, i56-i62.
[20] Alhakmi, G.; Assani, A.; Saadi, M.; Ammari, L. E.; A new mixed-valence lead(II) manganese(II/III) phosphate(V): $PbMn^{II}_2Mn^{III}(PO_4)_3$, *Acta Cryst*, **2013**, E69, i40-i46.
[21] Assani, A.; Saadi, M.; Alhakmi, G.; Houmadi, E.; Ammari, L. E.; $BaMn^{II}_2Mn^{III}(PO_4)_3$, *Acta Cryst.*, **2013**, E69, i60-i65.
[22] Ouaatta, S.; Assani, A.; Saadi, M.; Ammari, L. E. Crystal structure of calcium dinickel(II) iron(III) tris(orthophosphate): $CaNi_2Fe(PO_4)_3$ *Acta Cryst.*, *2017*, E73, 893-895.
[23] Ben Smail, R.; $K_{1+2x}Ni_{1-x}Fe_2(AsO_4)_3$ (*x* = 0,125): un nouvel arséniate à structure de type α-$CrPO_4$ *Acta. Cryst.*, **2017**, E73, 239-245.
[24] Ben Smail, R.; Zid, M. F.; An arsenate with the a-CrPO4 structure type, $NaCa_{1-x}Ni_{3-2x}Al_{2x}(AsO_4)_3$ (x = 0.23): crystal structure, charge-distribution and bond-valence sum analyses *Acta. Cryst.*, **2017**, C73, 896-904.
[25] Essehli, R.; Belharouak, I.; Ben Yahia, H.; Chamoun, R.; Orayech, B.; El Bali, B.; Bouziane, K.; Zhou, X. L.; Zhou, Z.; α-$Na_2Ni_2Fe(PO_4)_3$: a dual positive/negative electrode material for sodium ion batteries *Dalton Trans.*, **2015**, 44, 4526-4532.
[26] Harbaoui, D.; Sanad, M. M. S.; Rossignol, C.; Hlil, E. K.; Amdouni, N.; Obbade, S.; Synthesis and Structural, Electrical, and Magnetic Properties of New Iron−Aluminum Alluaudite Phases β-Na2Ni2M(PO4)3 (M = Fe and Al) *Inorg. Chem.*, **2017**, 56, 13051-13061.
[27] Avdeev, M.; Hester, J.R. ECHIDNA: a decade of high-resolution neutron powder diffraction at OPAL. *J. Appl. Cryst.* **2018,** 51, 1597–1604.
[28] Rietveld, H. M. Line profiles of neutron powder diffraction peaks for structure refnement *Acta Cryst.*, **1967**, 22, 151-152.
[29] Carvajal, J. R.; AN INTRODUCTION TO THE PROGRAM FULLPROF, July 2001.
[30] Lufaso, M. W.; Woodward, P. M.; Jahn-Teller distortions, cation ordering and octahedral tilting in perovskites *Acta Cryst.*, **2004**, B60, 10-20.

[31] Angenault J., Couturier J.C., Souron J.P., Siliqi D., Quarton M. The martensitic nature of the transition monoclinic ↔rhombohedral of $LiSn_2(PO_4)_3$ *Journal Of Materials Science Letters **1992***, 11 1705-1707
[32] Gagné, O. C.; Hawthorne, F. C. Comprehensive derivation of bond-valence parameters for ion pairs involving oxygen *Acta Cryst.* **2015**, B71 562–578.
[33] Brown, I. D.; Altermatt, D. Bond-valence parameters obtained from a systematic analysis of the inorganic crystal structure database *Acta Cryst*. **1985,** B41, 244–247.
[34] Nespolo, M., Ferraris, G.; Ohashi, H., Charge distribution as a tool to investigate structural details: meaning and application to pyroxenes, *Acta Cryst*. **1999**, B55, 902– 916.
[35] Nespolo, M., Isobe, M., Iida, J.; Kimizuka, N., Crystal structure and charge distribution of $YbFeMnO_4$ *Acta Cryst.*, **2000**, B56, 805–810.
[36] Nespolo, M., Ferraris, G., Ivaldi, G.; Hoppe, R., Charge distribution as a tool to investigate structural details. II. Extension to hydrogen bonds, distorted and hetero-ligand polyhedra *Acta Cryst*., **2001**, B57, 652–664.
[37] Guesmi, A., Nespolo, M.; Driss, A., Synthesis, crystal structure and charge distribution of $Na_7As_{11}O_{31}$: An oxygen-deficient layered sodium arsenate *J. Solid State Chem.*, **2006**, 179, 2466–2471.
[38] Eon, J.-G.; Nespolo, M. Charge distribution as a tool to investigate structural details. III. Extension to description in terms of anion-centred polyhedra *Acta Cryst*., **2015**, B71, 34–47.
[39] Nespolo, M., CHARDI-2015 (2015). http://www.crystallography.fr/ chardi.
[40] Nespolo, M.; Guillot, B., *CHARDI2015*: charge distribution analysis of non-molecular structures *J. Appl. Cryst*. **2016**, 49, 317–321.
[41] Baur, W.H. The geometry of polyhedral distortions. Predictive relationships for the phosphate group *Acta Crystallogr*. **1974**, B30, 1195-1215.
[42] Donnay, G.; Allman, R.; How to recognize O^{2-}, OH^-, and H_2O in crystal structures determined by x-rays *Am. Mineral.*, **1970**, 55, 1003-1015.
[43] Benarafa, L.; Rghioui, L.; Nejjar, R.; Saidi Idrissi, M.; Knidiri, M.; Lorriaux, A.; Wallart, F. Etude théorique et expérimentale des spectres de vibration des phosphates $K_3Ln(PO_4)_2$ *Spect. Chim. Acta*, **2005**, A61, 419-430.
[44] Tomaszewski, P. E.; Maczka, M.; Majchrowski, A.; Waśkowska, A.; Hanuza, J. Crystal structure and vibrational properties of $KMg_4(PO_4)_3$ *Solid State Sci.*, **2005**, 7, 1201-1208.
[45] Müller, A.; Krebs, B. Normal coordinate treatment of XY_4-type molecules and ions with T_d symmetry: Part I. Force constants of a modified valence force field and of the Urey-Bradley force field *J. Mol. Spectr.*, **1967**, 24, 180-197.
[46] Baran, E. J.; Roncaglia, D. I.; Infra-red spectra of α-$CrPO_4$-type phases *Spect. Chim. Acta*, **1988**, 44A, 399-401.
[47] Capitelli F., Dridi N., Arbib E.H, Valentini V. and Mattei G. New monodiphosphate $Li_9Cr_3(P_2O_7)_3(PO_4)_2$: X-ray crystal structure and vibrational spectroscopy*IZ. Kristallogr*. **2007**, 222, 521–526
[48] A. Ait Salah, P. Jozwiak, K. Zaghib, J. Garbarczyk, F. Gendron, A. Mauger, C.M. Julien FTIR features of lithium-iron phosphates as electrode materials for rechargeable lithium batteries *Spectrochimica Acta Part A* **2006**, 65, 1007–1013
[49] Kauffmann, T. H.; Kokanyan, N.; Fontana, M. D. Use of Stokes and anti-Stokes Raman scattering for new applications *J. Raman Spectrosc.*, **2018**, 1-7.

[50] Ouni, I. B.; Chapron, D.; Aroui, H.; Fontana, M. D.; Thermal behavior of high-frequency optical phonons in tetragonal $BaTiO_3$ single crystal *Appl. Phys. A*, **2016**, 122, 480-490.
[51] Ferrari, C. A.; Salzberg, J. B.; Luzzi, R. Polaron effects in resonant Raman scattering *Solid State Comm.*, **1974**, 15, 1081-1083.
[52] McCary, K. F.; Liu, J. Z.; Shelton, R. N.; Radousky, H. B. Raman-active phonons of a twin-free $YBa_2Cu_3O_7$ crystal: A complete polarization analysis *Phys. Rev*. **1990**, B41, 8792-8797.
[53] David, W. I. F.; Harrison, W. T. A.; Gunn, J. M. F.; Moze, O.; Soper, A. K.; Day, P.; Jorgensen, J. D.; Hinks, D. G.; Beno, M. A.; Soderholm, L.; Capone, D. W.; Schuller, I. K.; Seger, C. U.; Zhang, K.; Grace, J. D. Structure and crystal chemistry of the high-T_c superconductor $YBa_2Cu_3O_{7-x}$ *Nature*, **1987**, 327, 310-312.
[54] Khan, I.; Panini, P.; Khan, S. U. D.; Rana, U. A.; Andleeb, H.; Chopra, D.; Hameed, S.; Simpson, J. Exploiting the Role of Molecular Electrostatic Potential, Deformation Density, Topology, and Energetics in the Characterization of S···N and Cl···N Supramolecular Motifs in Crystalline Triazolothiadiazoles *Cryst. Growth Des.*, **2016**, 16, 1371−1386.
[55] Spasojević-De Biré, A.; Kiat, J. M. Electron deformation density studies of perovskite compounds *Ferroelectrics*, **1997**, 199, 143-158.
[56] Sakai, Y.; Oshibe, T.; Miyoshi, E. Theoretical study of the deformation densities of d electrons in K2 $[PdCl_6]$ and $K_2[PtCl_6]$ crystals *Acta Cryst.*, **1996**, B 52, 251-259.
[57] Takazawa, H.; Ohba, S.; Saito, Y.; Sano, M. Electron-density distribution in crystals of $K_2[MCl_6]$ (*M* = Re, Os, Pt) and $K_2[PtCl_4]$ at 120 K *Acta Cryst.*, **1990**, B46, 166-174.
[58] Turner, M. J.; McKinnon, J. J.; Wolff, S. K.; Grimwood, D. J.; Spackman, P. R.; Jayatilaka, D.; Spackman, M. A. *CrystalExplorer17*. The University of Western Australia, 2017.
[59] Jayatilaka, D.; Grimwood, D.J.; Tonto: A Fortran Based Object-Oriented System for Quantum Chemistry and Crystallography Comput. Sci. ICCS, 2003, 4, 142-151. 54
[60] Jayatilaka, D.; Grimwood, D.J.; Lee, A. TONTO-A System for Computational Chemistry University of Western Australia, Nedlands, 2005.

"For Table of Contents Only"

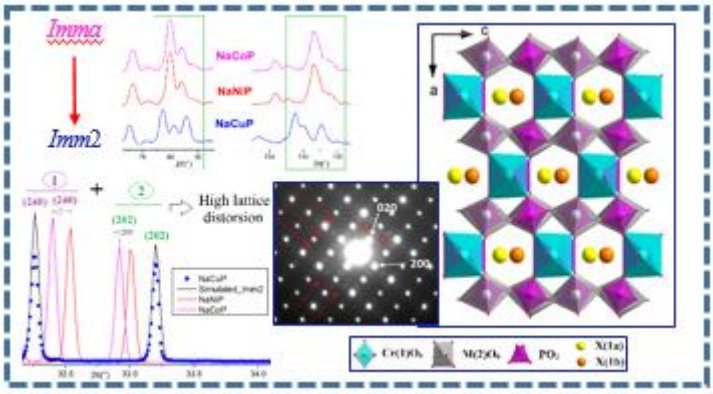

Synopsis : Combination of X-ray powder diffraction, neutron powder diffraction and electron diffraction allow us to suggest a noncentrosymmetric *Imm*2 space group for synthetic copper / chromium phosphate $NaCuCr_2(PO_4)_3$ (NaCuP) belonging to the well known α-$CrPO_4$ type.